5

Clouds and Precipitation

Extreme Rainfall and Rain from Shallow Clouds

Yukari N. Takayabu[1] and Hirohiko Masunaga[2]

[1]Center for Climate System Research, University of Tokyo, Kashiwa, Chiba, Japan
[2]Hydrospheric Atmospheric Research Center, Nagoya University,
Forocho Chikusa-ku, Nagoya, Japan

Abstract

This chapter reviews present knowledge on extreme precipitation and moderate rainfall from low-level clouds. Primary focus is on the statistics of precipitation characteristics rather than on a detailed description of individual case studies. First, observed variability of precipitation from low-level clouds and the existing techniques to separate different microphysical stages from remote-sensing measurements are reviewed. Over the tropical areas of Pacific and Atlantic oceans, the global distribution of shallow rainfall exhibits a "butterfly" pattern. This feature encompasses heavily precipitating regions such as the intertropical, south Pacific, and south Atlantic convergence zones (ITCZ, SPCZ, and SACZ, respectively); the northern hemispheric counterpart of SPCZ and SACZ emerges only when shallow rain is isolated.

The nature of extreme precipitation varies temporally. On a timescale of about a day, extreme precipitation is associated with synoptic-scale disturbances, including a notable example known as tropical plumes or moist conveyer belt, which could give rise to extreme daily precipitation in downstream arid regions. On an hourly timescale, extreme precipitation is caused by mesoscale moisture convergence, which is so intense that it maintains a continuous overturning of saturated air. Satellite observations imply that the global distribution of extreme precipitation shows a systematic difference from the total rainfall map in terms of, for example, the contrast between land and ocean. The distribution of low-level, precipitation-related latent heating associated with warm rain coincides with the butterfly pattern. Its cohabitation and separation with the deep heating suggests that warm rain plays a role in providing a thick layer of moist static energy source to the convection, and that it is also related to the tropical plumes which cause extreme precipitation in the semiarid west coasts of continents.

Precipitation from Low-level Clouds

Low-level clouds are typically non-precipitating, or just lightly precipitating, and are thus unlikely to cause hazardous weather events. Nevertheless, precipitation from low-level clouds is important meteorologically and climatologically for the following reasons: Precipitation from stratocumulus has a direct impact on the dynamic maintenance of its parent cloud (Nicholls 1984). In terms of the so-called second indirect effect of aerosols, an increase in aerosol concentration is hypothesized to suppress cloud droplet growth, leading to a longer cloud lifetime as the cloud drizzles out less efficiently (Albrecht 1989). Precipitation from stratocumulus clouds can thus be a controlling factor of the Earth's radiation budget, although they do not necessarily make a crucial contribution to global water cycle. Tropical and subtropical shallow cumulus yield significant precipitation through warm rain processes. Short and Nakamura (2000) estimated that shallow rainfall accounts for more than 20% of the total rainfall over tropical oceans.

Precipitation from low-level clouds comes generally in the form of warm rain, except in cases where a very low surface temperature does not allow cloud droplets to exist in the liquid phase. The microphysical processes involved in warm rain are relatively well understood (e.g., Mason 1952). Cloud droplets begin to grow in size, initially through vapor condensation to liquid water in supersaturated air. Condensational droplet growth is followed by the drizzling stage, onset by collision and coalescence with distinctly large droplets (20–100 μm) in a turbulent cloud layer. Drizzle turns to warm rain as the droplet coalescence proceeds further and precipitation rate increases.

A number of field campaigns with airborne probes have provided opportunities to study the microphysical properties of clouds in detail. *In-situ* measurements need to be complemented, however, by wide-area observations, such as satellite remote sensing, to obtain robust climatological evidence of large-scale variability. Yet how can we diagnose a microphysical condition from miles away, relying only on information carried by radiation emitted or scattered by cloud particles? To address this concern, let us look at some of the current remote-sensing methodologies used to detect cloud microphysical characteristics and discuss the global climatology of drizzle and shallow rain.

Regional and Global Observations of Drizzle and Warm Rain

Cloud Optical Thickness versus Effective Droplet Radius

Cloud droplets are distributed around 5–10 μm in radius, so that the geometrical optics approximation is valid for cloud droplets at visible wavelengths. Cloud optical thickness, τ_c, measured remotely in the visible (0.65 μm wavelength) spectrum is thus a practical proxy of the second moment of the cloud droplet size distribution integrated over the whole cloud layer:

$$\tau_c \approx 2\pi \int dz \int dr \; n(r)r^2, \qquad (5.1)$$

where z, r, and $n(r)$ denote the cloud layer depth, cloud droplet radius, and droplet size distribution, respectively. To translate τ_c into a parameter of meteorological relevance, such as liquid water path (LWP):

$$\text{LWP} \equiv \frac{4}{3}\pi\rho_w \int dz \int dr \; n(r)r^3, \qquad (5.2)$$

where $\rho_w = 1$g cm^{-3} is the liquid water density, conversion from observed τ_c to LWP requires knowledge on the relation between the second and third moments of $n(r)$. Combining Equations 5.1 and 5.2:

$$\text{LWP} \equiv \frac{2}{3}\rho_w\tau_c r_e, \qquad (5.3)$$

where

$$r_e \equiv \frac{\int dr \; n(r)r^3}{\int dr \; n(r)r^2}, \qquad (5.4)$$

and r_e is the effective droplet radius, representing the area-weighted average of cloud droplet radius. Nakajima and King (1990) established a methodology to retrieve cloud optical thickness and effective droplet radius from visible and near-infrared (typically at 3.7 μm) radiances.

The joint use of τ_c and r_e allows different microphysical stages to be separated. LWP increases with r_e and τ_c while cloud droplet number concentration remains nearly constant during the condensational droplet growth. By contrast, the subsequent stage promoted by droplet coalescence is not accompanied by an appreciable increase in LWP. Cloud optical thickness reduces with increasing r_e when LWP is unchanging or is only weakly changing, as inferred from Equation 5.3. The optical thickness versus effective radius diagram constructed from airborne remote sensing (Nakajima and Nakajima 1995) shows a clear contrast between drizzling and non-drizzling clouds as they vary from one area to another. Figure 5.1 shows a pair of sample plots representing both extreme cases. Figure 5.1a depicts clouds that stay at the condensational growth stage, where τ_c and r_e are positively correlated with each other. The correlation turns to negative in Figure 5.1b, implying that droplet collision and coalescence are at work. A very similar evolutionary track in the τ_c-r_e plane is obtained by a bin-microphysical model simulation (Suzuki et al. 2006; see also Nakajima and Schulz, this volume). The effective droplet radius does not reach 15 μm for non-drizzling clouds (Figure 5.1a), whereas r_e can be as large as 20 μm for drizzling clouds (Figure 5.1b). A number of studies, including airborne probe measurements and bin-microphysical model calculations, concluded independently that the transition from the condensational to collisional growth, or the initiation of drizzle, occurs when effective droplet radius reaches about 15 μm (e.g., Gerber 1996; Pinsky and Khain 2002).
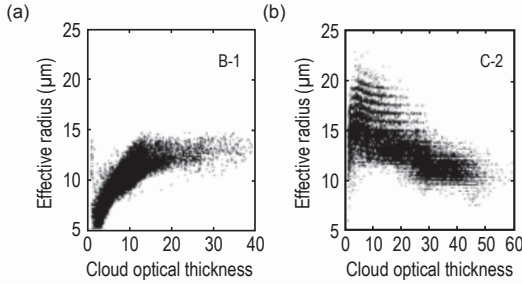
(a)   (b)

Figure 5.1   Scatterplot of τ_c and r_e for two observed scenes representing different microphysical states (adapted from Nakajima and Nakajima 1995).

Effective Droplet Radius versus Cloud-top Temperature

Within ascending moist air, cloud droplets grow in size so that droplet size increases generally with height inside a cloud layer. The droplet size at cloud top, however, is not uniquely determined for a given cloud thickness. For example, a high concentration of cloud condensation nuclei (CCN) could suppress drizzling for a cloud that otherwise develops deep enough to precipitate. Rosenfeld and Lensky (1998) demonstrated that the cloud-top temperature (T_c) versus an r_e diagram delineates closely the microphysical evolution that occurs in deepening clouds; it relies on the assumption that the local statistics of T_c and r_e are representative of various stages of a developing cloud. Case studies performed by Rosenfeld and Lensky (1998) were successful in identifying the distinct variation of cloud microphysics from one area to another in satellite imagery. Deepening clouds are occasionally not accompanied with significant droplet growth below the level at which droplets freeze (Figure 5.2a, b). In contrast, there are regions where clouds are allowed to reach immediately the drizzling threshold of $r_e = 15$ μm (Figures 5.2c, d). Rosenfeld and Lensky (1998) hypothesized that this contrast results from the difference in aerosol environment between continental and maritime air. The aerosol influence on clouds, as inferred by Rosenfeld and Lensky (1998) and their subsequent papers, remains controversial (see Ayers and Levin, this volume).

Cloud-top Droplet Radius versus Layer-averaged Droplet Radius

Droplet size increases with height toward the cloud top in non-precipitating clouds; however, the vertical gradient in droplet size should be counteracted by drizzle and rain drops falling toward the cloud base soon after the onset of precipitation. This change in vertical gradient is potentially useful to identify observationally the cloud microphysical stages. The vertical gradient of r_e is, however, not directly observable from the satellite-based schemes introduced above, given that infrared and near-infrared radiation do not penetrate deeply into a cloud layer. In contrast, a liquid cloud can be thoroughly scanned by
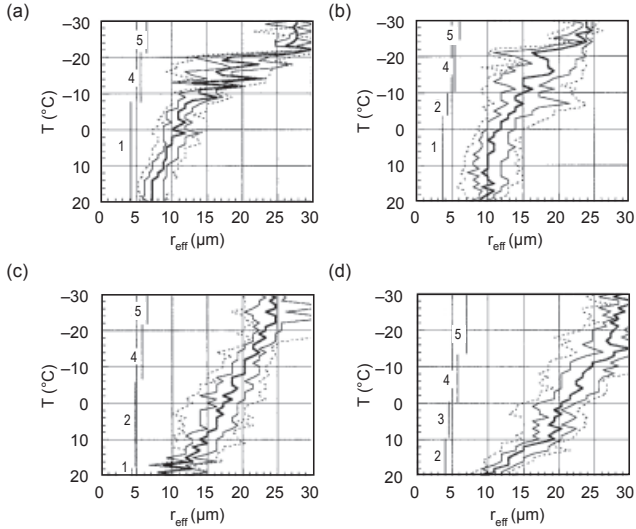
Figure 5.2 Local correlation between T_c and r_e for selected scenes. Different lines are 10th, 25th, 50th, 75th, and 90th percentiles of the r_e for each 1°C interval. Five microphysical stages: (1) condensational growth zone, (2) collisional growth zone, (3) rainout zone, (4) mixed-phase zone, and (5) glaciated zone. Panels (a) and (b) are constructed from continental scenes, and (c) and (d) are from maritime scenes. Adapted from Rosenfeld and Lensky (1998).

microwave radiation, to which cloud water is far less absorptive. Masunaga et al. (2002) proposed a technique to analyze the vertical inhomogeneity in droplet size by the combined use of a visible/infrared imager and a microwave radiometer. In their algorithm, a cloud layer-averaged r_e (or r_e^{ave}) is derived from Equation 5.3 with microwave-retrieved LWP and visible-retrieved τ_c. At the same time, cloud-top r_e (or r_e^{top}) is estimated using the Nakajima and King (1990) method. The partial beam-filling effect in microwave radiometry is corrected using the cloud fraction within a microwave field of view, which is determined from collocated visible radiance. Areas with cloud fractions lower than one-third are excluded from the analysis so that the retrieval noise that results from the uncertainties in surface microwave emission is kept at a minimum. Error analysis and further details in the methodology may be found in Masunaga et al. (2002). Target clouds are limited to those with top temperatures warmer than 273 K.

The global distributions of r_e^{ave} and r_e^{top} are shown in Figure 5.3. The two different versions of effective droplet radius share a common overall pattern, except that the variability of r_e^{ave} is significantly larger in amplitude than r_e^{top}. The effective droplet radii are greatest in the tropical convergence zones, where r_e^{ave} exceeds significantly the drizzling threshold or 15 μm, indicative of the frequent occurrence of warm rain. An intriguing feature is a northern mirror image of the SPCZ, which extends from the equatorial west Pacific
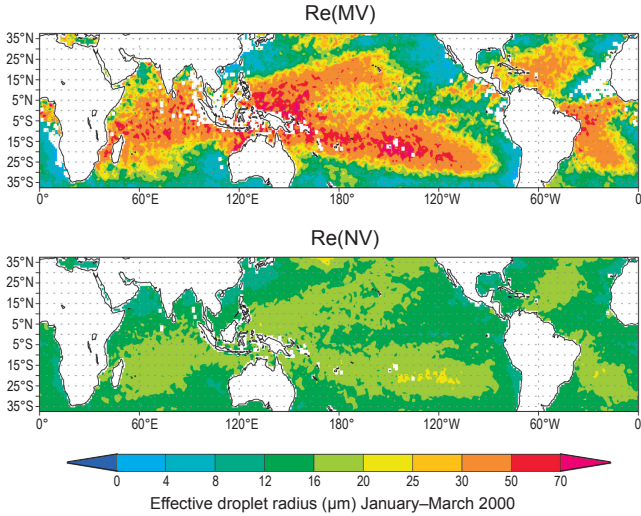
Re(MV)

Re(NV)

Effective droplet radius (μm) January–March 2000

Figure 5.3 The monthly mean global distribution of r_e^{ave} (top) and r_e^{top} (bottom) for January to March, 2000. Adapted from Masunaga et al. (2002).

to the northeast near Hawaii. A similar "butterfly" pattern is observed also in the Atlantic Ocean. A pair of similar butterfly wings is observed in shallow rain climatology (discussed later), whereas the southern wing overwhelms the northern counterpart in magnitude when precipitation from deep clouds is included.

There are areas where effective droplet radius does not reach the drizzling threshold. Particularly notable are subtropical oceans near the western coasts of major continents and the East China Sea, where r_e^{ave} is even smaller than r_e^{top}. The droplet growth in low-level clouds may be suppressed for a number of reasons including high lower-tropospheric stability (Klein and Hartmann 1993) and high aerosol concentration (Twomey 1977; Albrecht 1989). From their analysis of r_e^{ave} and r_e^{top}, Matsui et al. (2004) confirmed that the extent to which the drizzling and warm rain processes proceed is systematically correlated with both lower-tropospheric stability and aerosol concentration. The impacts of static stability and aerosols on low clouds are discussed individually in greater detail elsewhere in this volume (e.g., Bretherton and Hartmann; Feingold and Siebert).

Spaceborne Cloud-profiling Radar

CloudSat, which was launched in 2006, contains W-band (94 GHz) cloud-profiling radar (CPR) and has literally brought a new dimension to our ability to observe clouds from space. As a part of the A-Train constellation, CloudSat is particularly useful when combined with passive sensors on other satellites

flying in formation. Stephens and Haynes (2007) have attempted to estimate the droplet coalescence rate based on radar reflectivity observed by CPR together with τ_c and r_e retrieved by MODIS. Suzuki and Stephens (2008) devised a method to separate observationally the condensational growth stage and coalescence stage by a combined use of CPR reflectivity and r_e^{ave} evaluated from the MODIS and AMSR-E. More studies proposing new ideas that exploit the CloudSat and A-Train capabilities are expected in the future.

Global Climatology of Shallow Rain

Shallow cloud tops do not sharply contrast the background surface in satellite infrared imagery. Microwave radiometry is not sensitive either to the depth of a cloud or precipitation layer for a given LWP. It is therefore difficult, in principle, to isolate shallow rain through conventional satellite remote sensing. A breakthrough was brought about by the Tropical Rainfall Measuring Mission (TRMM) precipitation radar (PR), which is able to profile directly the vertical structure of precipitation. Short and Nakamura (2000) analyzed globally PR echo-top height (or storm height) and found that shallow cumulus constitute a distinct peak in the storm height histogram over tropical and subtropical oceans. In this section, we present the global climatology of shallow rain constructed from the 9-year TRMM PR observations: 1998–2006. We analyze the monthly PR near-surface rainfall projected on a half-degree global grid stored in the TRMM 3A25 dataset. Shallow rain is defined as those cases where echo-top heights are substantially lower than the freezing level. According to the TRMM product convention, shallow rain is divided into the two subcategories (isolated and non-isolated), depending on whether or not there is more developed precipitation nearby. As such, non-isolated shallow clouds are presumably a part of organized precipitation systems, such as mesoscale convective systems and tropical cyclones. PR sensitivity (> 17–18 dBZ) to drizzle and light rain (< 1 mm hr^{-1}) is marginal, so that shallow precipitation estimated from PR measurements is attributed mainly to warm rain from (relatively developed) shallow convective clouds. We note that there is so little precipitation from stratocumulus and thus it is not observable in the results below.

In Figure 5.4a, b, monthly rainfall is shown from isolated shallow clouds for February and August, respectively. Isolated shallow clouds precipitate most heavily over subtropical oceans as well as in the ITCZ. The overall global distribution is reminiscent of that for cloud droplet radius (Figure 5.3). The "butterfly" pattern mentioned earlier is again observed in the Pacific and Atlantic oceans. Non-isolated shallow rain (Figures 5.4c, d) contrasts clearly in spatial distribution with the isolated shallow rain. Whereas non-isolated shallow cumulus is, in general, tightly concentrated near the cores of the tropical convergence zones, isolated shallow clouds prefer the fringes of the convergence zones or are outside of the zones, as pointed out by Schumacher and Houze (2003). Non-isolated shallow cumulus can be greater in rain rate than isolated
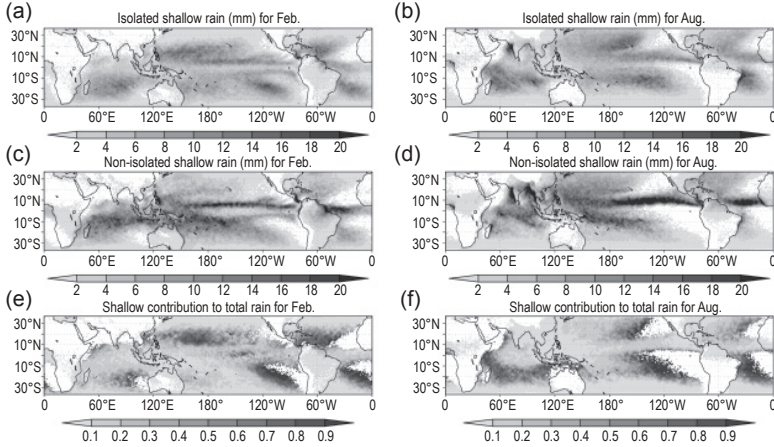
Figure 5.4   The climatology of monthly rainfall from shallow isolated clouds for February (a) and August (b), constructed from the TRMM PR 3A25 dataset. Shallow non-isolated rain is shown in (c) and (d), with the same parameters; (e) and (f) show the ratio of shallow rain (with both isolated and non-isolated) to the total precipitation.

shallow clouds, but the shallow cumulus contribution to total precipitation is only secondary in the tropical convergence zones (Figure 5.4e, f). In contrast, shallow rain explains more than 90% of the total precipitation in several limited regions, including the subtropical oceans, particularly in the winter hemisphere, and at the eastern edge of the SPCZ and SACZ. All of these regions are located under a subsiding branch of the Hadley and Walker circulations, accompanied by a relatively warm sea surface. The strong inversion in such areas hampers deep convection from developing and traps moisture supplied from the underlying ocean, which allows shallow clouds to predominate.

Figure 5.4 shows that there is very little warm rainfall from shallow cumulus over tropical continents compared to tropical oceans, except for the Amazon basin in the wet season (Figure 5.4c). The factors that suppress continental shallow precipitation include (but may not be limited to) the abundance of aerosols acting as CCN and relatively limited moisture supply over land.

Summary

The observed characteristics of large-scale variability in precipitation from low-level clouds have been described. Such observations require a remote-sensing technique to separate drizzling and raining clouds from non-precipitating clouds. Three existing methods were reviewed that utilize (a) cloud optical thickness and effective droplet radius, (b) cloud-top temperature and effective droplet radius, and (c) layer-top and layer-averaged effective droplet radii. Results from these analysis methods are consistent with our knowledge of the low-cloud properties that we have gained from *in-situ* observations in

past decades. Satellite observations have shown systematic variability in cloud microphysical status over a wide range of spatial scales beyond the reach of individual field campaigns. Satellite data analysis reveals a large-scale gradient in low-level cloud properties from the deep tropics, where shallow rain occurs frequently, toward the subtropical western coasts of major continents, typical of maritime stratocumulus with little precipitation.

Layer-averaged effective droplet radius is as large as 50 μm or even larger, indicating a frequent occurrence of warm rain in broad areas across the tropical and subtropical oceans. Such areas include not only the ITCZ, SPCZ, and SACZ but also the northern hemisphere counterparts of SPCZ and SACZ. The predominance of shallow rainfall over the northern hemispheric subtropical oceans in February and the southern Indian Ocean in August is confirmed by TRMM PR measurements. Rich moisture supply from warm sea surface and the prevalence of strong trade inversion are presumably major factors that make these regions favorable to shallow rainfall. We do not, however, fully understand why such conditions appear in a quasi-symmetric "butterfly" pattern. In contrast, the tropical convergence zones, which geographically constrain deep convective rainfall, are highly asymmetric about the equator.

As mentioned earlier, precipitation from low-level clouds is not at all hazardous. Shallow rainfall may, however, contribute thermodynamically to extreme precipitation events. Below, we will discuss the possibility that lower tropospheric moistening by shallow clouds could play a role in the development of deeper and more organized convective systems.

Extreme Rainfall

In view of the impact of climate change on human society, changes in extreme rainfall are as important as changes in total rainfall, especially in terms of disaster prevention. It has often been pointed out that while global atmospheric moisture increases with a warming climate (as diagnosed from the Clausius–Clapeyron equation) ~6.5% per Kelvin, projections from climate models indicate that the change in global mean precipitation would be 3.4% per Kelvin. This discrepancy is understood in the context of energy balance, as global mean precipitation is constrained by the atmospheric radiative cooling rate rather than the atmospheric moisture content (e.g., Hartmann and Larson 2002). It is also suggested that while the mean precipitation does not increase at the rate of the atmospheric moisture content, frequency of extreme precipitation would increase more significantly.

Karl et al. (1995) analyzed long-term trends in the daily precipitation station data over the United States, the former Soviet Union (FSU), and China. They found a significant increase in the annual proportion of extreme precipitation category (>50.8 mm d^{-1}) over the U.S. for the period of 1911–1994, although the proportions of moderate (12.7–25.4 mm d^{-1}) and light precipitation

categories (2.54–12.7 mm d^{-1}) decreased. A summertime increase in extreme precipitation exceeded 2% of the total summer precipitation; this corresponds to an average of adding one extreme event every two years. They also noted that this increase did not result from an increase in intensity but rather to an increase in the number of days. Over the FSU or China, little systematic change was found in precipitation variability.

In this section, we provide an overview of the future projection of extreme rainfall in climate models. To address current understanding of extreme rainfall, we discuss individual phenomena related to extreme rainfall and emphasize that it cannot be defined without considering temporal or spatial scales.

Extreme Rainfall and Future Change from a Climate Model Perspective

What is "extreme rainfall"? One can easily imagine how the same level of precipitation, 50 mm d^{-1}, can be viewed differently in the wet monsoon region versus in the semiarid subtropics. Certainly, it cannot be defined with one global threshold of rainfall intensity. Thus to address the issue of representing extreme rainfall in the climate models, local values of extreme precipitation (e.g., 20-yr return values of annual extremes of 24-hr precipitation) are often utilized.

Using six climate model experiments, future changes in dynamic and thermodynamic components of mean and extreme precipitation were examined separately by Emori and Brown (2005). For extreme precipitation, the multiyear mean of the fourth largest value was utilized at each grid point. Emori and Brown showed that the global mean change of average precipitation for the 2081–2100 A1B scenario, run from 1981–2000, was 6%, while that for extreme precipitation was as large as 13%. Most of the extreme precipitation change resided in the thermodynamic component, which showed an overall increase even for the areas of modest change or decreasing mean precipitation. They postulated that with a moister atmosphere, the same amounts of mass convergence or divergence results in larger moisture convergence and divergence, and that this brought about larger increases in extreme precipitation.

Kharin et al. (2007) examined extreme precipitation with a 20-yr return period in an ensemble of global coupled climate models as part of the IPCC diagnostic exercise for the Fourth Assessment Report. For future projections of extreme precipitation, multi-model median 20-yr return values of daily precipitation increase with SRES A1B experiment was 6–7% per Kelvin, which was close to the projected Clausius–Clapeyron rate, while the corresponding mean precipitation change was 3.4 % per Kelvin. This result was also consistent with the study by Emori and Brown (2005). Kharin et al. noted that the simulated present-day precipitation extremes were plausible in the extratropics, but in the tropics, large intermodel discrepancies existed. Uncertainties in the tropics were very large, not only in the models but also in the available reanalysis

data for comparison, and this abated the confidence in the projected changes in extreme precipitation.

State-of-the-art climate model results suggest strongly that some physical processes associated with extreme precipitation are not well represented in the models, especially over the tropics. Although most model studies on extreme rainfall are based on daily precipitation, we must be mindful that "extremes" vary largely, depending on temporal scales of phenomena as well as the temporal resolution of data. Next we review the observations to examine what phenomena contribute to the extreme precipitation in different temporal resolutions.

Extreme Rainfall from Observational Aspects

Figure 5.5 shows the depth–duration relationships of the world record rainfalls and Japanese record rainfalls, based on precipitation data collected by Jennings (1950) and plotted by Ninomiya and Akiyama (1978, pers. comm.). Depending on the temporal scale, changes in record points indicate that various types of heavy precipitation systems have contributed to rainfall accumulation records on different temporal scales. On a scale of annual to ten days, record precipitation is found in Cherrapunji (northeast India). On a scale of a week to one day, accumulation is greatest in the tropics. From one day to 30 minutes, record levels are found in the subtropics, whereas for less than one hour, record precipitation occur in the midlatitudes and tropics.
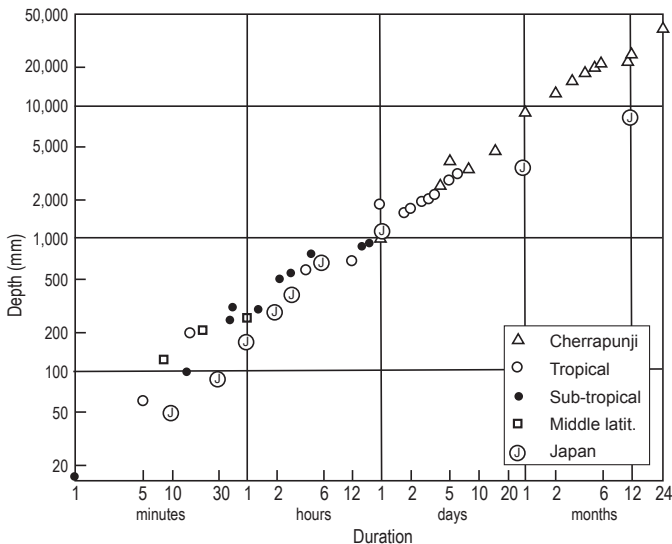

Figure 5.5   Depth–duration relationships of the world record rainfalls and Japanese record rainfalls. Adapted from Ninomiya and Akiyama (1976).

Trenberth (1999) stressed the importance of understanding the change in precipitation that is associated with different types of storms, and recommended that hourly precipitation datasets be collected. Below, we present examples of how various types of storms contribute to extreme precipitation in different regions and on different temporal scales.

Tropical–Extratropical Interactions

Several studies suggest that extreme precipitation occurs over the arid or semiarid regions, along the west coasts of continents, in association with tropical–extratropical interactions. Higgins et al. (2000) utilized 3-day accumulations of precipitation data along the West Coast of the U.S. and found that extreme precipitation events occur during neutral winters just prior to the onset of El Niño. This is a period when intraseasonal activity is large in the tropical Pacific. Jones (2000) examined the daily precipitation in California and showed that frequency of extreme events are more common when tropical convective activity associated with the Madden-Julian Oscillation is high.

Extreme daily precipitation during the winter in the semiarid southwestern U.S., as analyzed by Higgins et al. (2000) and Jones (2000), is related to the enhancements of tropical plumes (i.e., bands of clouds that extend from the deep tropics into subtropical and midlatitudes and last only a few days) (McGuirk et al. 1988; Knippertz and Martin 2007). Figure 5.6 provides an example of the eastern Pacific tropical plume captured by the infrared image from GOES West. Knippertz and Martin (2007) showed that the tropical plume or the "moist conveyer belt" enhances the water vapor fluxes above the planetary boundary layer at around 700 hPa, and causes potential instability in concert with the overriding dry air.
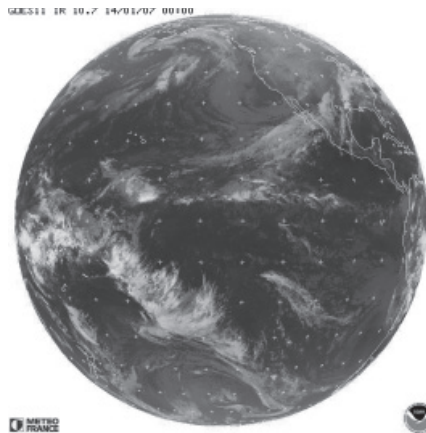

Figure 5.6 An example of the tropical plume over the eastern Pacific, captured in the infrared image of GOES West at 00z January 14, 2007. Obtained from http://www.satmos.meteo.fr/cgi-bin/qkl_sat/quicklook.pl

Tropical plumes are also observed in association with extreme precipitation in arid northwest Africa. Knippertz and Martin (2005) examined three cases of extreme rain over western Africa. For two cases, precipitation exceeded half of the local climatological annual precipitation within just a few days. The other case exceeded the corresponding monthly climatological value. Associated with the deepening of the extratropical trough into the tropics, a tropical plume was observed, which transported moisture in the middle (~600 hPa) level, to produce a potentially unstable stratification in which convection could begin.

Extreme Rain in Japan Associated with the Baiu Front

Japan is located in a region that is subjected to exceptionally heavy rainfall for its latitude. Figure 5.5 shows the rainfall accumulation records for Japan on different timescales. As can be seen, the observed levels of rainfall from several hours to one-day accumulation in Japan are comparable to corresponding world records. This is because extreme rain, which is associated with mesoscale precipitation systems, occurs frequently over Japan, because it is located in a moist subtropical region affected both by subtropical active frontal and depression systems and tropical moist air masses. We note that a similar environmental condition is present in the southeast U.S.

Ninomiya and Akiyama (1978) examined the distributions of rainfall extremes in Japan on different temporal scales and found that the meridional gradient in extreme 10-min accumulated rainfall distribution was small. It was similar to the gradient of the total precipitable water content. They showed that the 10-min rainfall record value corresponded to the maximum precipitable water (~50 mm/10 min) in the atmosphere, or one overturning of the saturated atmosphere. From this point of view, hourly accumulated rainfall represents how many times the moist atmosphere is overturned, or how effective the mesosystems can gather the moisture into the convection. Assuming the typical spatial scale of the extreme rainfall with 50 mm/10 min to be 10^4 km^2, an area of 6×10^4 km^2 needs to be contracted into 10^4 km^2 in one hour to realize the extreme hourly precipitation of 300 mm hr^{-1}. This corresponds to the convergence of about 2×10^{-4} sec^{-1}, which is the typical value of the mesoscale systems. Thus, it is estimated that a continuous overturning for one hour (~300 mm hr^{-1}) is possible with the existence of mesoscale systems. Moreover, distribution of hourly extremes showed a larger meridional gradient compared to the 10-min extremes. This is most likely attributable to the oceanic southerly flow, which prepares a more effective moisture convergence in mesoscale systems, but is not yet limited to particular geographical locations.

Daily extremes, however, were found to be relatively locked into geographic locations. In contrast to hourly rainfall records, the daily extreme value is far from a continuous overturning of the moist atmosphere: There is no ~7200 mm day^{-1} precipitation, and since large-scale disturbances cannot

gather moisture as effectively, daily extremes consist of intermittent recovery of mesoscale systems.

Intense Thunderstorms Observed from TRMM

Short-term extreme precipitation is considered to be associated with intense thunderstorms. Employing various kinds of indices obtained from the precipitation features (PFs) database, Zipser et al. (2006) used satellite observations from TRMM to describe the global distribution of extremely intense thunderstorms. Figure 5.7 shows the distributions of extreme (uppermost 0.01% frequency) PFs with different indices. It is indicated that the most extreme PFs are observed over Equatorial Africa, southeastern U.S., and southeast South America. During the months of March–May and June–August, extreme PFs are found in the southeastern area of Africa, northern and eastern areas of India
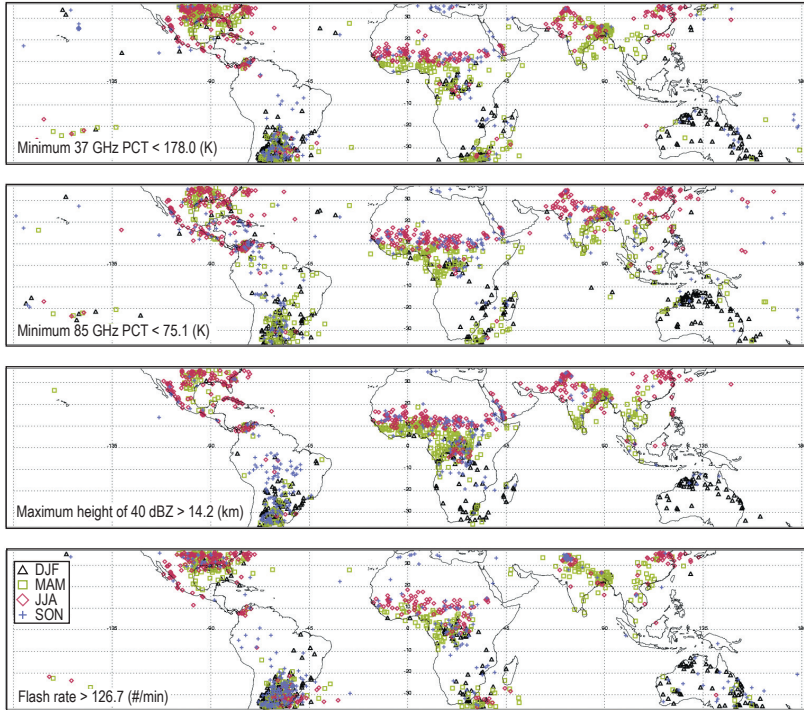

Figure 5.7　Seasonal cycle of the extreme categories with a threshold of 0.01 % occurrences for different parameters obtained from the precipitation feature database. The top two panels are based on minimum precipitation from TRMM microwave observations with the frequency of 37 GHz and 87 GHz, respectively. The third panel is based on the TRMM precipitation radar reflectivity with a threshold of maximum height of 40 dBZ > 14.2 km. The bottom panel is based on the TRMM LIS observations with flash rate > 126.7 min^{-1}. Adapted from Zipser et al. (2006).

and Indochina, and eastern China, whereas from December–February PFs are found in the northern part of Australia. Extremely intense thunderstorms are distributed very differently from total rainfall amount for which regions (e.g., Amazon and the Maritime Continent) would be dominant. These distributions of extreme events correspond instead to the distributions of intense mesoscale convective complexes.

Takayabu (2006) calculated rainyield per flash (RPF) values with the TRMM precipitation radar and lightning imaging sensor (LIS) data. RPF is the total rainfall normalized with lightning flash numbers; thus, it represents the rainfall characteristics irrespective of the rainfall amount. Figure 5.8 presents the 8-year mean distribution of RPF and the average rainfall rate. Regions of most intense thunderstorms are indicated with dark shades of small RPF values. Above all, a strong contrast of RPF between land and ocean is seen, consistent with the observations that most thunderstorms are observed over land. This feature is in contrast with the average rainfall rate, which exhibits rather continuous distribution of tropical rain bands over ocean and over land. The distribution of extremely small RPF values corresponds well to that of extreme PF events in Figure 5.7 over Equatorial Africa, southeastern U.S., southeastern South America, along the periphery of the Tibetan Plateau, and the northern part of Australia. It is also readily observed that regions of largest total annual
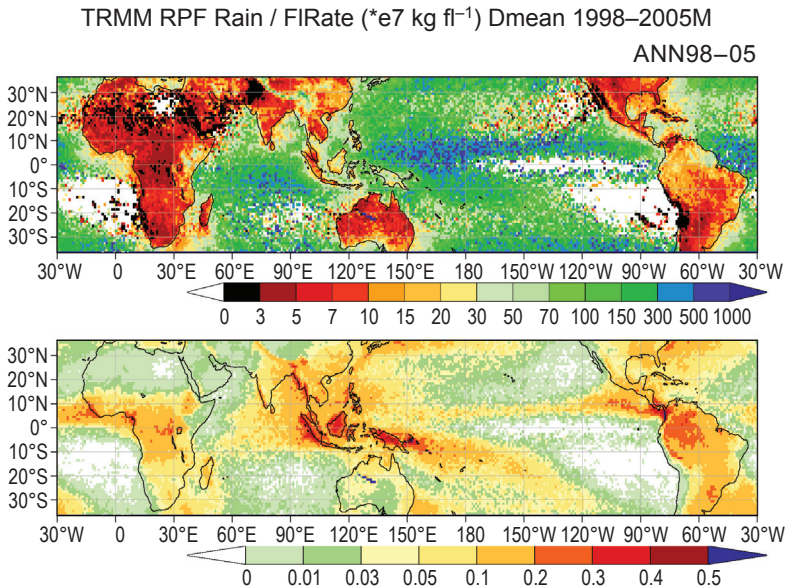

Figure 5.8 Global distributions of 8-yr mean rain yield per flash (a) and unconditional mean rain rate averaged throughout the period (b). Units for the color scales are 10^7 kg fl^{-1} for (a) and mm hr^{-1} for (b). Rain yield per flash averages are obtained by dividing the total precipitation amount by the total flash number for the averaging period.

precipitation, such as Amazonia and the Maritime Continent, are secondary in terms of intensity of the thunderstorms with small RPF values. This is consistent with Zipser et al.'s (2006) conclusions. The overall correspondence of rain characteristics, represented by RPF and PFs, indicate that satellite observations effectively detect extreme rain associated with intense mesoscale convective systems, the distribution of which differs from accumulation extremes which occur over a few days.

Discussion

Thus far, extreme rainfall addressed in climate models has been based primarily on daily precipitation. However, recent satellite observations are able to detect effectively the extreme rainfall associated directly with the mesoscale convective systems. As suggested by prior studies (e.g., Ninomiya and Akiyama 1978; Trenberth 1999; Knippertz and Martin 2005), extreme hourly precipitation corresponds to intense mesoscale systems, whereas extreme daily precipitation is controlled by larger synoptic-scale systems. We must recognize that factors controlling the intensity of synoptic-scale systems and mesoscale systems are entirely different. There has been a discussion with climate model simulations that increasing rate of the extreme rainfall is proportional to the increase of atmospheric moisture. However, while the mesoscale systems' convergence can attain the amount of continuous atmospheric overturning, synoptic-scale convergence cannot maintain continuous overturning. Therefore, when daily extreme precipitation is considered, we must treat both the atmospheric moisture content as well as adequate representations of synoptic-scale systems as essential. Although the assumption may be correct that atmospheric moisture content affects extreme rainfall more directly than the total rainfall amount, quantitative conclusions with daily rainfall extremes require reexamination.

Finally, we wish to discuss the relationship between shallow convection and deep and intense convection. Figure 5.9 shows the distribution of convective heating in terms of Q1–QR, defined by Equation 5.5, at 7.5 km and 2.0 km, respectively, for the December–February season averaged for nine years of TRMM observation. This was calculated with the spectral latent heating (SLH) algorithm introduced by Shige et al. (2004). Q_1 is called as the apparent heating (Yanai et al. 1973),

$$Q_1 \equiv \frac{D\overline{s}}{Dt} = \frac{\partial \overline{s}}{\partial t} + \overline{v} \bullet \nabla \overline{s} + \overline{\omega} \frac{\partial \overline{s}}{\partial p} = Q_R + L(\overline{c} - \overline{e}) - \nabla \bullet \overline{s'v'} - \frac{\partial \overline{s'\omega'}}{\partial p} \quad (5.5)$$

where $s = CpT + gz$, overbars represent large-scale values and primes represent eddy values. L is the latent heat of vaporization, Q_R is the atmospheric radiative heating, c is the condensation rate, and e is the evaporation rate, where Cp is the heat capacity for a constant pressure, T is the temperature, and gz is the geopotential. Note that these two altitudes are typical for cold and warm

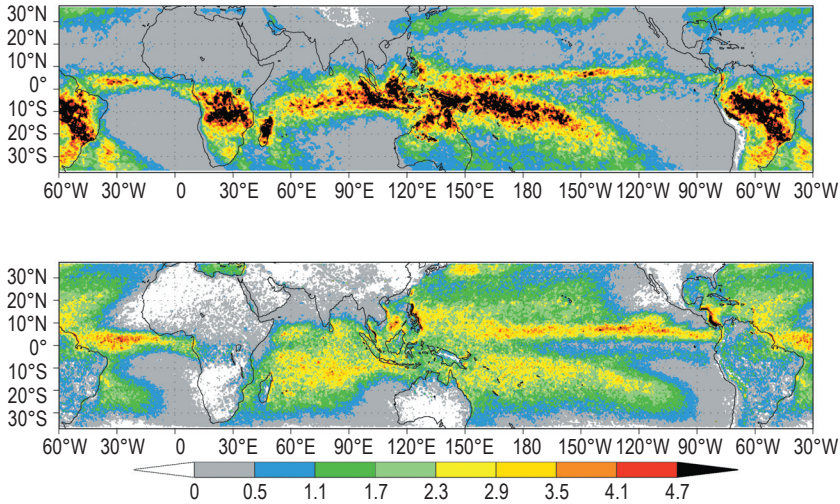UncondMean Q1R 97–06 DJF Lev: 7.5 km, 2.0 km & OISSTv2

Figure 5.9 Global distributions unconditional mean Q1–QR (apparent heat source minus the radiative heating) averaged for December–February seasons of 1997–2005. Upper panel (a) shows those at the level of 7.5 km and the lower panel (b) is for the 2.0 km. Unit in the gray scale is K d^{-1}.

rainfall, corresponding to two peaks appearing in the average heating profile. From the SLH tables, it is also known that the 2 km heating peak corresponds to the 4–5 km rain top height (not shown).

The distribution of the taller (7.5 km) heating looks similar to the familiar total rainfall distribution. The shallower (2.0 km) heating distribution corresponds to that shown in Figure 5.4 for shallow clouds, and indicates some differences from the distribution of taller heating. There is a more distinct land–sea contrast, and shallow heating is observed almost exclusively over ocean and not much over land, except for over land in the Maritime Continent region. Many studies suggest the importance of preconditioning with the shallow convection to moisten the lower troposphere, prior to the mature convection of oceanic large-scale organized convective systems. Over the Indian Ocean, the western Pacific warm pool, ITCZ, and SPCZ, it is apparent that tall and shallow convective heating coexist. In these regions, shallow convection is considered to prepare the moist lower troposphere for tall convection to start.

There are, however, particular regions where shallow heating is ubiquitous but not the taller heating. These regions are found where the sea surface temperature is relatively high and at the periphery of the subtropical high pressure area latitudes. One region is located in the northern wing of the "butterfly shape" of shallow clouds, extending from the western Pacific warm pool toward the Hawaii Islands (discussed above). A corresponding northern wing

without taller heating is also found from the western to central Atlantic. Since the 2.0 km heating peak corresponds to warm rain with 4–5 km rain top height in SLH tables, the lower troposphere is moistened with this shallow convection over these regions, whereas tall convection is suppressed by the subsidence under the influence of subtropical highs. It is interesting to notice that the two tropical plume regions mentioned earlier, over the eastern Pacific and over the Atlantic, extend from the eastern ends of these northern wings to the arid and semiarid continents. It is reported that the axis of moisture transport by tropical plumes is 600–700 hPa and that it originates from moderate convection, which seems to correspond to the warm rain observed here. Tropical plumes bridge lower to middle tropospheric moisture from the warm rain region over the arid and semiarid continents.

In conclusion, these results suggest that a realistic reproduction of synoptic systems as well as a proper representation of shallow convection and its interaction with synoptic-scale systems are indispensable if we wish to reproduce extreme daily precipitation adequately.

References

Albrecht, B. A. 1989. Aerosols, cloud microphysics, and fractional cloudiness. *Science* **245**:1227–1230.

Emori, S., and S. J. Brown. 2005. Dynamic and thermodynamic changes in mean and extreme precipitation under changed climate. *Geophys. Res. Lett.* **32**:L17706.

Gerber, H. 1996. Microphysics of marine stratocumulus clouds with two drizzle modes. *J. Atmos. Sci.* **53**:1649–1662.

Hartmann, D. L., and K. Larson. 2002. An important constraint on tropical cloud–climate feedback. *Geophys. Res. Lett.* **29**:1951.

Higgins, R. W., J.-K. Schemm, W. Shi, and A. Leetmaa. 2000. Extreme precipitation events in the western United States related to tropical forcing. *J. Climate* **13**:793–820.

Jones, C. 2000. Occurrence of extreme precipitation events in California and relationships with the Madden-Julian Oscillation. *J. Climate* **13**:3576–3587.

Karl, T. R., R. W. Knight, and N. Plummer. 1995. Trends in high-frequency climate variability in the twentieth century. *Nature* **377**:217–220.

Kharin, V. V., F. W. Zwiers, X. Zhang, and G. C. Hegerl. 2007. Changes in temperature and precipitation extremes in the IPCC ensemble of global coupled model simulations. *J. Climate* **20**:1419–1444.

Klein, S. A., and D. L. Hartmann. 1993. The seasonal cycle of low stratiform clouds. *J. Climate* **6**:1587–1606.

Knippertz, P., and J. E. Martin. 2005. Tropical plumes and extreme precipitation in subtropical and tropical West Africa. *Q. J. Roy. Meteor. Soc.* **131**:2337–2365.

Knippertz, P., and J. E. Martin. 2007. A Pacific moisture conveyor belt and its relationship to a significant precipitation event in the semiarid southwestern United States. *Wea. Forecast* **22**:125–144.

Mason, B. J. 1952. Production of rain and drizzle by coalescence in stratiform clouds. *Q. J. Roy. Meteor. Soc.* **78**:377–386.

Masunaga, H., T. Y. Nakajima, T. Nakajima et al. 2002. Physical properties of maritime low clouds as retrieved by combined use of tropical rainfall measuring mission microwave imager and visible/infrared scanner: Algorithm. *J. Geophys. Res.* **107(D10)**:4083.

Matsui, T., H. Masunaga, and R. A. Pielke, Sr. 2004. Impact of aerosols and atmospheric thermodynamics on cloud properties within the climate system. *Geophys. Res. Lett.* **31**: L06109.

McGuirk, J. P., A. H. Thompson, and J. R. Schaefer. 1988. An eastern Pacific tropical plume. *Mon. Wea. Rev.* **116**:2505–2521.

Nakajima, T., and M. D. King. 1990. Determination of the optical thickness and effective particle radius of clouds from reflected solar radiation measurements. Part I: Theory. *J. Atmos. Sci.* **47**:1878–1893.

Nakajima, T. Y., and T. Nakajima. 1995. Wide-area determination of cloud microphysical properties from NOAA AVHRR measurements for FIRE and ASTEC regions. *J. Atmos. Sci.* **52**:4043–4059.

Nicholls, S. 1984. The dynamics of stratocumulus: aircraft observations and comparisons with a mixed-layer model. *Q. J. Roy. Metetor. Soc.* **110**:783–820.

Ninomiya, K., and T. Akiyama. 1978. Characteristics of torrential rain in Japan, observed from its intensity and the moisture budgets. Research report No.A-53-4 for the Special Research on Natural Disasters. Tokyo: Mext.

Pinsky, M. B., and A. P. Khain. 2002. Effects of in-cloud nucleation and turbulence on droplet spectrum formation in cumulus clouds. *Q. J. Roy. Meteor. Soc.* **128**:501–534.

Rosenfeld, D., and I. M. Lensky. 1998. Satellite-based insights into precipitation formation processes in continental and maritime convective clouds. *Bull. Amer. Meteor. Soc.* **79**:2457–2476.

Schumacher, C., and R. A. Houze, Jr. 2003. The TRMM precipitation radar's view of shallow, isolated rain. *J. Appl. Meteor.* **42**:1519–1524.

Shige, S., Y. N. Takayabu, W.-K. Tao, and D. E. Johnson. 2004. Spectral retrieval of latent heating profiles from TRMM PR data. Part 1: Development of a model-based algorithm. *J. Appl. Meteor.* **43**:1095–1113.

Short, D. A., and K. Nakamura. 2000. TRMM radar observations of shallow precipitation over the tropical oceans. *J. Climate* **13**:4107–4124.

Stephens, G. L., and J. M. Haynes. 2007. Near global observations of the warm rain coalescence process. *Geophys. Res. Lett.* **34**:L20805.

Suzuki, K., T. Nakajima, T. Y. Nakajima, and A. Khain. 2006. Correlation pattern between effective radius and optical thickness of water clouds simulated by a spectral bin microphysics cloud model. *SOLA* **2**:116–119.

Suzuki, K., and G. L. Stephens. 2008. Global identification of warm cloud microphysical processes with combined use of A-train observations. *Geophys. Res. Lett.* **35**:L08805

Takayabu, Y. N. 2006. Rain-yield per flash calculated from TRMM PR and LIS data and its relationship to the contribution of tall convective rain. *Geophys. Res. Lett.* **33**:L18705.

Trenberth, K. E. 1999. Conceptual framework for changes of extremes of the hydrological cycle with climate change. *Climate Change* **42**:327–339.

Twomey, S. 1977. The influence of pollution on the shortwave albedo of clouds. *J. Atmos. Sci.* **34**:1149–1152.